Secondary antiproton flux induced by cosmic ray interactions with the atmosphere

C. Y. Huang,* L. Derome, and M. Buénerd†
Laboratoire de Physique Subatomique et de Cosmologie, IN2P3/CNRS, 53 Av. des Martyrs, 38026 Grenoble cedex, France
(Received 20 May 2003; published 29 September 2003)

The atmospheric secondary antiproton flux is studied for detection altitudes extending from sea level up to about three earth radii, by means of a three-dimensional Monte Carlo simulation, successfully applied previously to other satellite and balloon data. The calculated antiproton flux at mountain altitude is found to be in fair agreement with the recent BESS measurements. The flux obtained at balloon altitude is also in agreement with calculations performed in previous studies and used for the analysis of balloon data. The flux at sea level is found to be significant. The antineutron flux is also evaluated. The antiproton flux is prospectively explored up to around 2×10^4 km from the Earth. The results are discussed in the context of the forthcoming measurements by large acceptance experiments.

DOI: 10.1103/PhysRevD.68.053008 PACS number(s): 94.30.Hn, 13.85.−t, 95.85.Ry, 96.40.−z

I. INTRODUCTION

The antiproton ($\bar{p}$) has a particular status in the spectrum of cosmic radiation mainly because of its particular production dynamics and kinematics. The main part of the cosmic ray (CR) $\bar{p}$ spectrum measured in balloon and satellite experiments is well accounted for by assuming that it consists of a secondary flux, originating from the interaction between the nuclear CR flux and the interstellar matter (ISM) in the galaxy [1]. It is expected to be dominant with respect to components from other possible origins. Other such contributions of primary origin and of major astrophysical interest have been considered recently. In particular, the $\bar{p}$ flux induced by annihilation of dark matter constituents [2–4] and by primordial black hole evaporation [5,6] has been discussed. All these possible contributions are intimately entangled together and their phenomenological disentangling relies critically on the accuracy of the experimental data. The measurements of the $\bar{p}$ flux thus provide a sensitive test of the production source and mechanism and of the propagation conditions in the galaxy [1,7–12].

CR antiprotons have been experimentally studied for several decades by satellite or balloon borne experiments (see references in [13]). Several recent balloon experiments, like BESS [14,15] and CAPRICE [13,16] have collected new data samples whose analysis has provided determinations of the galactic $\bar{p}$ flux over a kinetic energy range extending from about 0.2 GeV kinetic energy up to about 50 GeV. In this work, the values of the antiproton galactic flux were obtained by subtracting the calculated atmospheric $\bar{p}$ flux from the values of the measured total flux.

Secondary galactic as well as atmospheric antiprotons are both produced in hadronic collisions by the same elementary reaction mechanism in nucleon-nucleon collisions between the incident CR flux and either ISM nuclei (mainly hydrogen) in the galaxy or atmospheric nuclei (mainly nitrogen) in the atmosphere. The basic $\bar{p}$ production reaction is the inclusive $NN\rightarrow\bar{p}X$ process, N standing for the nucleon and X for any final quantal hadronic state allowed in the process. The ratio of $\bar{p}$ production in the galaxy and in the atmosphere scales with the ratio of matter thickness (in units of interaction length λ_I) crossed by protons in the two media. These thicknesses are known to be of the same order of magnitude. In addition, both fluxes are driven by similar transport equations (see [7,9,17,18] for example), with, however, the escape term arising from convective and diffusive effects in the interstellar medium on the galactic flux [7], making a significant difference from the transport of flux in the atmosphere, which tends to decrease the transported flux compared to the atmospheric transport conditions.

It can be shown using a leaky box model (LBM) for the galactic transport and a simple slab model for the production in the upper atmosphere [19] that the ratio of the atmospheric $\bar{p}$ flux at balloon altitude N_{atm} to the galactic $\bar{p}$ flux at the top of the atmosphere (TOA) N_{gal} is approximately

$$\frac{N_{atm}(\bar{p})}{N_{gal}(\bar{p})}\approx\frac{x_{atm}}{\lambda_e}\frac{\sigma(p(\mathrm{atm})\rightarrow\bar{p}X)}{\sigma(pp\rightarrow\bar{p}X)}\frac{m_{\mathrm{H}}}{m_{atm}}\approx\frac{x_{atm}}{\lambda_e}\left(\frac{m_{\mathrm{H}}}{m_{atm}}\right)^{1/3}.$$

Here x_{atm} is the thickness of the atmosphere on top of the balloon experiments, while λ_e is the LBM escape length, $\sigma(pp\rightarrow\bar{p}X)$ and $\sigma(p(\mathrm{Atm})\rightarrow\bar{p}X)$ being the inclusive antiproton production cross sections on hydrogen and on the atmospheric nuclei, respectively, while m_{H} and m_{atm} are the hydrogen and mean atmospheric nuclear mass, respectively. Using $x_{atm}=3.9$ g/cm^2 (for a 38 km altitude) [20] and $\lambda_e=8$ g/cm^2 and 11.8 g/cm^2 for particle rigidities of 3 GV and 10 GV, respectively [21], the above ratio is found to be of the order of 0.15 and 0.2, respectively. The contribution of the atmospheric antiproton production to the total flux measured in balloon experiments is thus not expected to be negligible with respect to the galactic component. The correction of the

*Present address: MPIK, Saupfercheckweg 1, D-69117 Heidelberg, Germany.
†Corresponding author. Electronic address: buenerd@in2p3.fr

total flux from the atmospheric contribution therefore needs the latter to be calculated very carefully, since the accuracy in the evaluation of this component sets a limit to the accuracy on the final value of the measured galactic flux.

It must be emphasized that studying the secondary proton flux in the atmosphere in this context also is interesting, since it is very sensitive to all the components of the simulation process, in particular to the secondary proton production cross section, which also contributes to the generation of the antiproton flux. Comparison of the calculation to the recently measured data provides a robust validation of the approach used and of the overall calculation, and firmly supports the reliability of the results reported here. This study is reported in a separate (companion) paper [22].

The present work is an extension of a research program aiming at the interpretation of satellite data and for which the first results on the flux of protons, leptons, and light ions, below the geomagnetic cutoff (GC), at satellite altitude, have been reported recently [23–25].

The paper reports on the calculated $\bar{p}$ atmospheric flux over the range from sea level up to satellite altitudes by Monte Carlo simulation. The main features of the calculations are described in Sec. II. The production cross sections used in the event generator are given in Sec. III. The results are discussed in Sec. IV. The work is concluded in Sec. V.

II. SIMULATION CONDITIONS

As mentioned above, the flux of secondary atmospheric antiprotons has been investigated using the same simulation approach, which has allowed one to successfully account for the p, d, He, and $e^{\pm}$ experimental fluxes below the geomagnetic cutoff measured by the AMS experiment, as well as the experimental proton and muon fluxes in the atmosphere, the latter being studied together with the atmospheric neutrino flux [26].

The same computing environment has been used here for charged particle propagation in the terrestrial environment, including the atmosphere, as in the previous studies, with the event generator being dedicated, however, based on the antiproton production cross section in nucleon-nucleon collisions.

The calculation proceeds by means of a full 3D simulation program. Incident cosmic rays are generated on a virtual sphere chosen at a 2000 km altitude. Random events are generated uniformly on this sphere. The local zenith angle distribution of the particle momentum is proportional to $\cos(\theta_z)d\cos(\theta_z)$, θ_z being the zenith angle of the particle, in order to get an isotropic flux at any point inside the volume of the virtual sphere. The geomagnetic cutoff is applied by back-tracing the particle trajectory in the geomagnetic field, and keeping in the sample only those particles reaching a back-tracing distance of ten earth radii. Flux conservation along any allowed particle path in the geomagnetic field is ensured by application of Liouville's theorem. The normal particle propagation as well as its back tracing are performed using the adaptative Runge-Kutta integration method in the geomagnetic field [26].

(1) For the incident CR proton and helium flux, functional forms fitted to the 1998 AMS measurements were used [27,28] (see also [29–31]). The heavier components of the CR flux were not taken into account in the calculations (see [26]). For other periods of the solar cycle, the incident cosmic fluxes are corrected for the different solar modulation effects using a simple force law approximation [32].

(2) Each particle is propagated in the geomagnetic field and interacts with nuclei of the local atmospheric density according to their total reaction cross section and producing secondary nucleons p,n, and antinucleons $\bar{p},\bar{n}$ with cross sections and multiplicities. This important issue is discussed in Sec. III below. The specific ionization energy loss is computed for each step along the trajectory.

(3) In the following step, each secondary particle produced in a primary collision is propagated in the same conditions as the incident CRs in the previous step, resulting in a more or less extended cascade of collisions through the atmosphere, which may include up to ten generations of secondaries for protons for the sample generated in this work [22,23].

For the antinucleon inelastic collisions, only the annihilation reaction channel was taken into account. Nonannihilating inelastic $\bar{N}+A\rightarrow\bar{N}+X$ ($\bar{N}$ standing for antinucleon) interactions whose contribution to the total reaction cross section σ_R is small have been neglected at this stage. It consists basically of a single diffractive dissociation cross section (for the proton target in individual $\bar{N}p$ collisions), and it would be of the same order of magnitude as for pp collisions, namely, $\sim 10\%$ of σ_R or less at the energies considered here [33]. It has been neglected at this stage. It will be included in further developments of the calculation program.

The reaction products are counted whenever they cross, upward or downward, the virtual detection spheres (several can be defined in the program) at the altitude of the detectors: from sea level up to about 36 km for ground and balloon experiments (BESS, CAPRICE) and 370 km for the AMS satellite experiment. Higher altitudes up to more than 10 000 km were also investigated, with the purpose of understanding the dynamics of the population of quasitrapped particles in the earth environment (see Sec. IV G). Each particle is propagated until it disappears by nuclear collision (annihilation for antinucleons), stopping in the atmosphere by energy loss, or escaping to the outer space beyond twice the generation altitude [23–26].

In the terminology used in the following, one event is defined as the full cascade induced by an incoming CR particle interacting with one atmospheric nucleus. For each CR producing at least one secondary particle, the whole event is stored with all the relevant topological, dynamical, kinematical, and geographical information. This includes the collision rank, geophysical location, altitude, momentum, particle type, and parent particle type, in the form of event files. The collision rank is defined as the number of a given collision in the cascade initiated by the first CR interaction with the atmosphere (rank 1).

The calculations do not include any adjustable parameters.

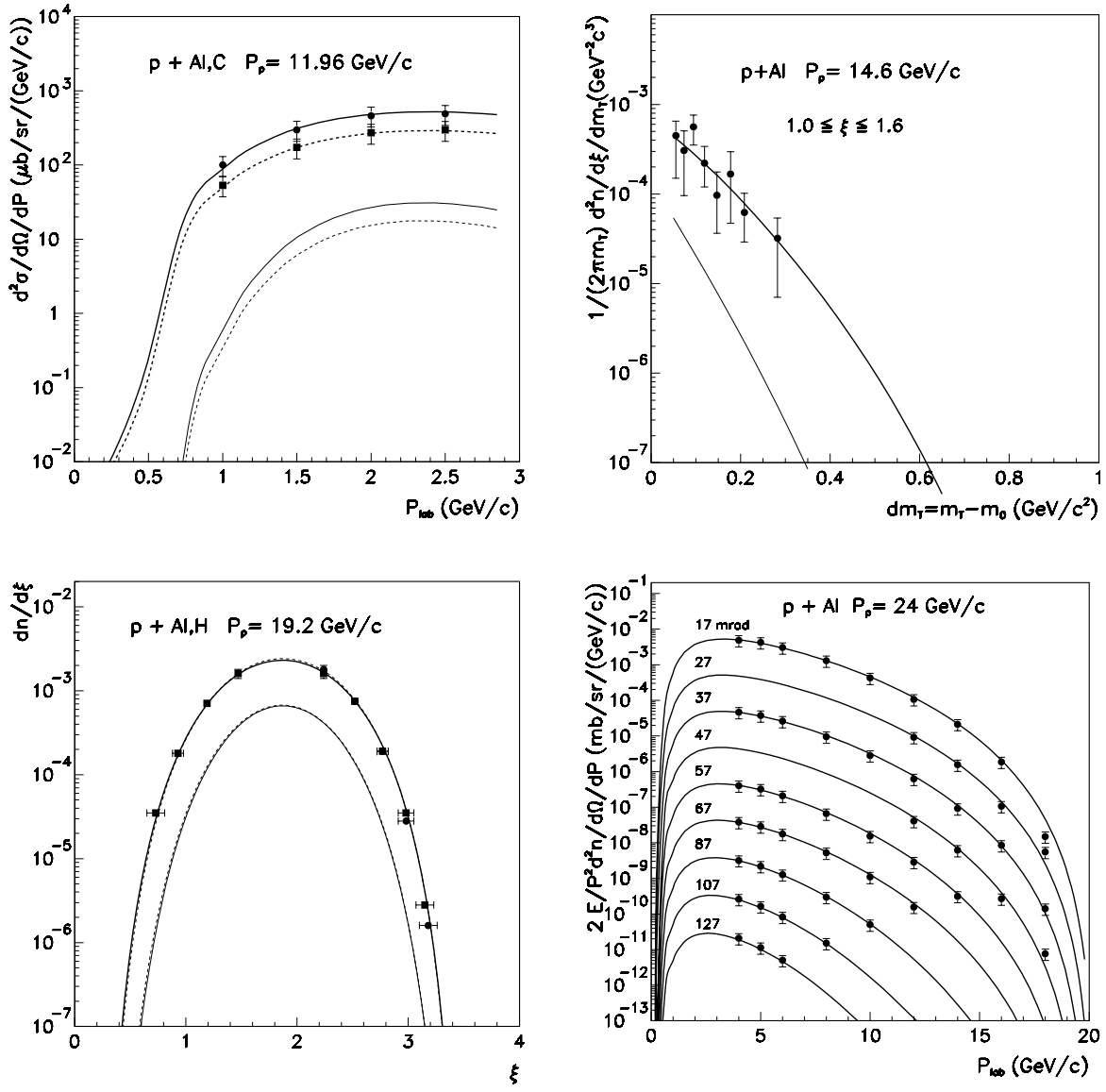

FIG. 1. Sample of the fits to the $p+A\rightarrow\bar{p}+X$ cross section data using the parametrized relation (1) given in the text, with the parameters of Table I [42]. Top left: Differential cross sections measured at 5.1° for $p+\mathrm{C}$ (full squares) and for $p+\mathrm{Al}$ (full circles) [37] as a function of the particle momentum, compared with fit using Eq. (1) (thick solid for Al and thick dashed for C), and using the KMN relation and parameters from [41] (thin solid and thin dashed, respectively). Top right: Same comparison for 14.6 GeV/c $p+\mathrm{Al}$ invariant differential cross section versus mass transfer from [38]: Fit with Eq. (1) (thick line) and KMN calculations [41] (thin line). Bottom left: Same for 19.2 GeV/c $p+p$ (full squares) and $p+\mathrm{Al}$ (full circles) rapidity distributions from [39]: fit with Eq. (1) (solid and dashed thick lines, respectively) and KMN calculations [41] (thin solid and dashed lines, respectively). Bottom right: 24 GeV/c $p+\mathrm{Al}$ invariant differential cross sections at various angles (in msr on the figure) from [40] compared to the fits with Eq. (1). For each measurement angle above the first (17 mrad), each next cross section has been multiplied by 10^{-1}, 10^{-2}, etc., for presentation purposes. KMN calculations are not shown on this figure for legibility. Note that the same definitions of cross sections have been used as in the original references. There is a clear target mass dependence of the differential cross section in the top left panel, while in the bottom left panel almost no such dependence is observed, because the observable displayed is a multiplicity, i.e., ratio of differential cross section to total reaction cross section.

III. CROSS SECTIONS

A. Proton induced secondaries

1. Protons

The inclusive $p+A\rightarrow p+X$ proton production cross sections used are described in Ref. [23]. They are based on the results of Refs. [34] and [35] for the two components corresponding basically to forward (or direct quasielastic) and backward (or relaxed deep inelastic) production, respectively. The values obtained have been found in reasonable agreement with the results of the Intra Nuclear Cascade Liège (INCL) model of intranuclear cascade calculations [36]. This cross section allows us to reproduce very successfully the atmospheric secondary proton flux down to the lowest altitude [22].

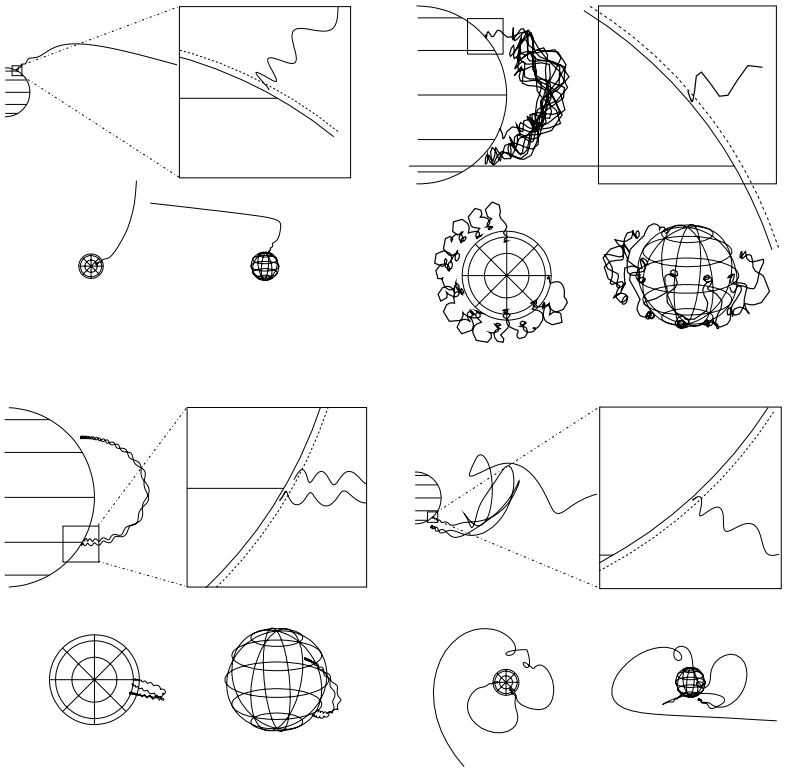

FIG. 2. Examples of antiproton trajectories in the earth's magnetic field. Details are discussed in the text.

The cross section for secondary neutron production was taken equal to that of proton production. Similarly, the neutron induced cross sections of secondary nucleon production were taken the same as for protons, the Coulomb interaction making negligible differences over the energy range considered.

2. Antiprotons

The inclusive $p+A\rightarrow\overline{p}+X$ antiproton production cross section has been obtained by fitting a set of available experimental data between 12 GeV incident kinetic energy and 24 GeV/c incident momentum [37–40], using a modified version of the analytical formula proposed in Ref. [41], the latter being referred to as the KMN (for Kalinovski, Mokhov, and Nikitin) formula in the following.

The invariant triple differential cross section is described by means of the formula used in [41]:

$$\left(E\frac{d^3\sigma}{d^3p}\right)_{\text{inv}}=\sigma_R C_1 A^{b(p_t)}(1-x)^{C_2}\exp(-C_3x)\Phi(p_t). \tag{1}$$

In this relation the kinematical variables p_t and x are the transverse momentum and the fractional energy of the particle, respectively, as defined in [41] [relation (3.26) in this reference], while σ_R is the total $p+A$ reaction cross section. The function $\Phi(p_t)$ was modified as

$$\Phi(p_t)=\exp(-C_4p_t^2)+C_5\frac{\exp(-C_6x_t)}{(p_t^2+\mu^2)^4}\exp(-\alpha\sqrt{s}) \tag{2}$$

with $b(p_t)=b_0\cdot p_t$ within the range of four-momentum transfer considered here. Figure 1 shows some of the results obtained [42] by fitting the set of available data studied for this work with relation (1). The energy dependent exponential factor in the second term of relation (2) was introduced because it was found that this term contributes only at low incident energy. The values of the parameters obtained are given in Table I. These values are significantly different from those given in the original work [42,43] on a smaller number of data. This work is currently being extended up to 400 GeV incident proton energy [44].

B. ^{4}He induced secondaries

1. Protons

The inclusive $^4\text{He}+A\rightarrow p(n)+X$ proton (neutron) production cross section was obtained as described in Sec. III A 1 above for the $p+A\rightarrow p+X$ cross section (using the total reaction cross section from [45] for this system), renormalized to the available experimental multiplicities measured for this reaction [46,47].

2. Antiprotons

The inclusive antiproton production cross section was evaluated by means of the wounded nucleon model [48,49]

TABLE I. Values of the parameters of relation (1) obtained in fitting the data of Fig. 1.

Parameter	C_1	C_2	C_3	C_4	C_5	C_6	μ	b_0	α
Value	0.042	5.92	0.96	2.19	84.3	10.5	1.1	0.12	2.24

using the available experimental values of the total reaction cross sections for the ^{4}He$+A$ and $p+A$ systems, and of the $\bar{p}$ production multiplicity in nucleon-nucleon collisions [43].

In this model, the particle production multiplicity $\langle n_{AB}\rangle$ in the collision between nuclei A and B is related to the multiplicity in nucleon-nucleon ($\mathcal{N}\mathcal{N}$) collisions $\langle n_{\mathcal{N}\mathcal{N}}\rangle$:

$$\langle n_{AB}\rangle = \frac{1}{2}\left(A\frac{\sigma_{pB}}{\sigma_{AB}} + B\frac{\sigma_{pA}}{\sigma_{AB}}\right)\langle n_{\mathcal{N}\mathcal{N}}\rangle \qquad (3)$$

with σ_{ij} being the total reaction cross section between the i and j systems. Using this model, the $\bar{p}$ production multiplicity induced by the CR He component on the nitrogen N component of the atmosphere is found to be $\langle n_{\mathrm{HeN}}\rangle \approx 1.55\langle n_{pN}\rangle \approx 2.5\langle n_{PP}\rangle$.

C. Total reaction cross sections

Protons. The values of the proton total reaction cross sections on nuclei used were obtained from the parametrization of [50], and checked on the carbon data from [45].

^4He. The ^{4}He$+A$ total reaction cross sections used were taken from [45].

Antinucleons. The $\bar{p}$ total reaction cross section was taken from [51], with the energy dependence from the data compilation of [52]. The same production cross section and total reaction cross section have been assumed for $\bar{n}$ production as for $\bar{p}$.

IV. RESULTS

A sample of about 35×10^6 CRs have been simulated, of which 20% were effectively propagated to the atmosphere (above the GC), for detection altitudes going from sea level up to 10^4 km altitude, including the BESS/CAPRICE balloon altitude ($\approx$38 km), the AMS orbit altitude ($\approx$370 km), and the recent BESS measurement terrestrial altitude (2770 m). The flux at sea level was calculated to investigate the possibility of ground level measurement of atmospheric antiprotons with existing devices [53]. This was achieved independently by BESS at mountain altitude and the results are discussed below.

A. Particle trajectories in the earth's magnetic field

The time of confinement of particles in the earth environment together with their particular trajectories determine their status with respect to the three categories trapped, semitrapped, and nontrapped (escape). Trapped particles are spiraling back and forth around and along the magnetic field lines long enough to drift many times around the earth (see, for example, [54,55] and below). Trapped particles are not observed in practice in the energy domain considered here. They are not dynamically forbidden, however, and a few trajectories with a few 10^2 bounces are observed, which correspond to short-lived trapped particles. Quasitrapped particles are in similar kinematic conditions but accomplish only a limited number of bounces at mirror points before being absorbed or escaping (see examples below). This concept appeared during the first years of radiation belt studies

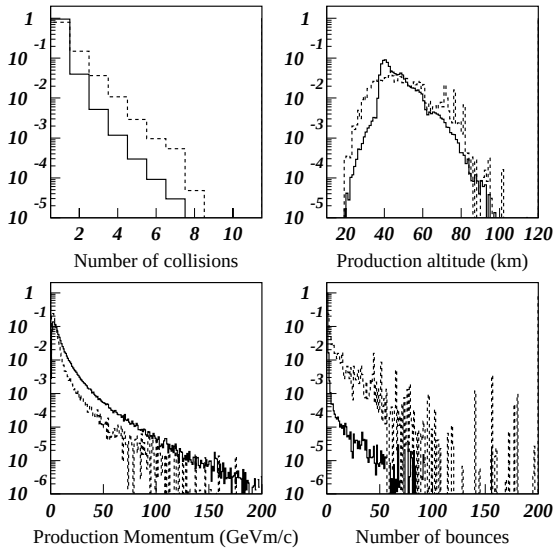

FIG. 3. General features of the simulated $\bar{p}$ sample at balloon (38 km) and satellite (380 km) altitudes. Top left: Rank distribution (see text). Top right: Altitudes of production. Bottom left: Momentum distributions. Bottom right: Numbers of bounces effected by the particle between the mirror points. The spikes observed for high bounce multiplicity in this distribution correspond to quasitrapped particle trajectories crossing the detection altitude many times.

[56] (see also the discussion in [54]). Escape particles do not match the kinematic conditions for being trapped at their production point and escape in a very short time to the outer space. All intermediate situations between the stereotypes of quasitrapped and escape trajectories are in fact observed in the simulation results (see example in the bottom left of Fig. 2).

Figure 2 shows four examples of characteristic trajectories of antiprotons generated in this study. The four panels give a side view (projection on the meridian plane, top left), side view zoomed around the production point showing the spiraling trajectory of the particle (top right), top view (projection on the equatorial plane, bottom left), and 3D representation (bottom right) of each of the selected trajectories.

The top left event (1.52 GeV kinetic energy) is an escape particle produced close to the North Pole. Top right is a semitrapped single bounce event (0.54 GeV) annihilating in the atmosphere close to its production point. Bottom left is a longer lifetime, multibounce, semitrapped event (2.48 GeV), drifting around the earth for about three-quarters of a turn before annihilation in the atmosphere in the region of the South Atlantic anomaly (SAA). Bottom right is intermediate between a semitrapped (since it displays at least one clear bounce) and an escape event (0.54 GeV). It is a type of event for which the first adiabatic invariant (magnetic moment conservation) is not conserved because of a large variation of the magnetic field along the radius of gyration [54].

B. General features of the simulated data

Figure 3 shows a few basic distributions of physics observables relevant to the dynamics of the process for two detection altitudes 38 km (solid line) and 380 km (dashed

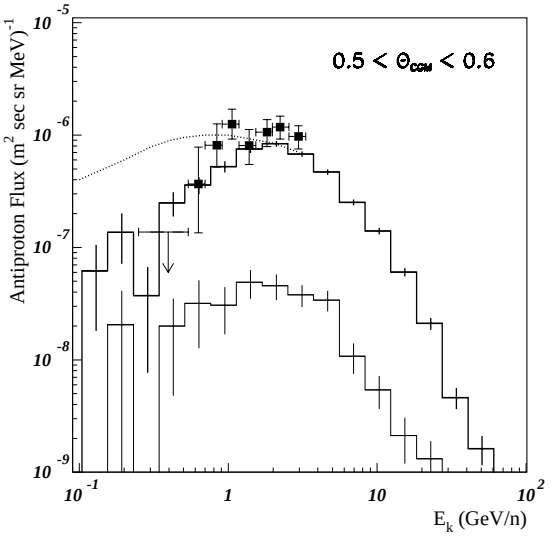

FIG. 4. Antiproton flux data at 2770 m measured by BESS [59] (symbols) compared with simulation results (histograms). Thick histogram: full calculation. Thin histogram: CR ^{4}He contribution. Dotted line: transport equation calculation from [61].

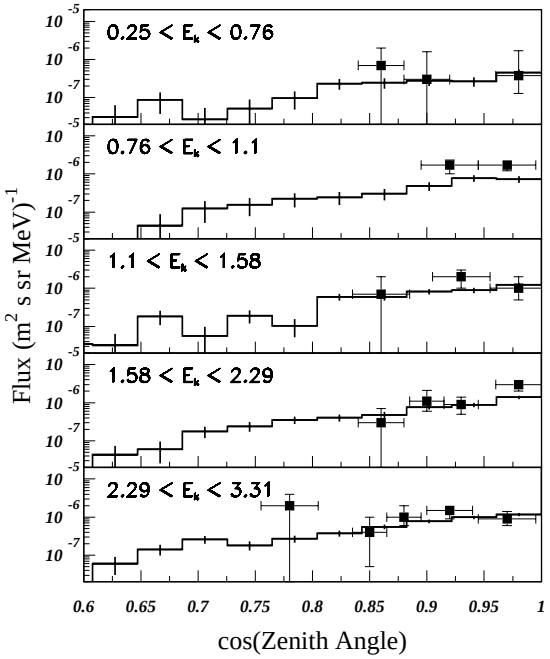

FIG. 5. Experimental zenith angle distribution of the antiproton flux at 2770 m in bins of kinetic energy compared with simulation results.

line) corresponding to balloon and satellite (AMS) altitudes, inside and outside the atmosphere, respectively. The rank of the collision producing the antiproton (top left panel on the figure) appears to extend from 1 up to about 10 for the simulated sample, showing that $\bar{p}$'s are produced up to the tenth generation in the collision cascade. The distributions are a little different for the two altitudes, with a significantly larger number of $\bar{p}$ occurring from the first interaction at the lower altitude. The altitude distribution of the production point for the detection at 38 km (top right) shows a discontinuity at this altitude due to the incoming flux dominated by production from the upper layer of the atmosphere. The mean production altitude is found around 46 km and 48 km for the lower and upper detection altitudes, respectively. The particle momentum spectrum at the production point (bottom left) is found to be harder at the higher altitude. The number of bounces at the mirror points for particle trajectories spiraling around the magnetic field lines are found, as expected, to be very different for the two altitudes of detection. At 38 km, only a small population is seen to reach a number of bounces larger than a few units (5–6). This flux is significant, however, and must correspond to trajectories lying mostly outside the atmosphere. At 380 km, the observed flux of $\bar{p}$ trajectories with more than one bounce is larger by about two orders of magnitude than at 38 km, corresponding to the population of quasitrapped particles as discussed previously in [23,58].

C. Antiproton flux at mountain altitude

The recent measurements of the $\bar{p}$ flux at 2770 m altitude by the BESS Collaboration [59] (see also [60]) allow us to perform a sensitive test of the ability of the present simulation program to account for the observed flux since at this altitude the $\bar{p}$ production occurs after a cascade of four collisions on the average (see the previous section and Fig. 3). Another highly sensitive test of the overall calculation is provided in [22] on the atmospheric proton flux.

Figure 4 shows the $\bar{p}$ spectrum at 2770 m of altitude measured by BESS, compared to the simulation results. The latter was run with the geometrical acceptance function of the BESS spectrometer given in [60] (Figs. 4.37–4.39; see also [62]), the overall acceptance angle being of the order of 25°. The total CR $p+$He and partial He fluxes are shown on the same figure. The He flux contribution is seen to produce a small fraction of about 5% of the full $\bar{p}$ flux. Although the total flux calculated slightly underestimates the experimental values, the overall agreement is quite good, the calculated values being on the average within one standard deviation from the experimental values. This gives confidence in the results of the calculations obtained for the other altitudes investigated and reported below.

Figure 5 compares the experimental zenith angle distributions of the $\bar{p}$ flux to the calculated values (histograms) for the same kinetic energy bins as measured by BESS [60]. On this figure, the overall agreement between data and calculations again appears to be good for all energy bins.

Note that no upward particles were produced at this altitude in the simulated sample, as could be expected [43].

D. Balloon data

In this section the atmospheric $\bar{p}$ flux at balloon altitude is investigated for comparison with the atmospheric $\bar{p}$ corrections made to the raw flux data in the BESS and CAPRICE experiments.

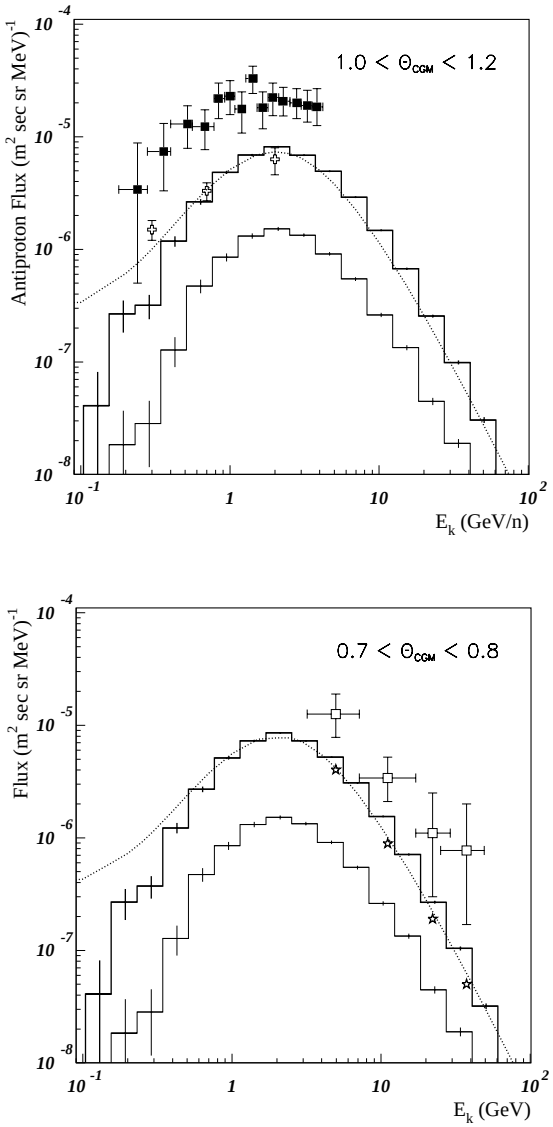

FIG. 6. Top: BESS results: Galactic antiproton distributions deduced from the data (full squares), atmospheric antiproton flux from Ref. [61] (curve), and corrections applied by the authors of [15] to correct the raw flux values for the atmospheric contribution in the original work (open crosses), compared with the atmospheric flux obtained in the present work; all CR proton + ^{4}He contributions (thick histogram); CR ^{4}He contribution (thin histogram). Bottom: Same for the CAPRICE experiment data [13] (open squares) and corrections applied in [13] (star symbols). In both panels Θ_{CGM} stands for the geomagnetic latitude of the measurements.

Figure 6 shows the values of the galactic $\bar{p}$ flux obtained from the BESS and CAPRICE measurements. These values were obtained from the measured raw flux by subtraction of the atmospheric $\bar{p}$ flux evaluated using an average of theoretical calculations for the BESS experiment [15], and using the calculations of Ref. [61] for CAPRICE. On the figure, the atmospheric flux calculated in [61] is compared with the results from the present work (see also [17]). For the two sets of data, it appears that the present calculations are in fairly good agreement with the atmospheric antiproton flux obtained from transport equation calculations and used to correct the measured raw flux. There is a slight trend, however, for the simulation results to be larger than those obtained from the differential equation approach by about 20% over the range 10–30 GeV. At low $\bar{p}$ energies the opposite trend is observed and the simulation results are found significantly below the values obtained from the differential equation. One might say that the simulation results should be taken with care below 1 GeV because of the lack of experimental cross sections for low energy $\bar{p}$ production, and thus the large corresponding uncertainties in the results of the simulation over this range; however, it must be noted that the calculated cross sections for low $\bar{p}$ momentum should be reliable in principle for the following reason. The $\bar{p}$ distribution is naturally symmetric in the rapidity space. The fitting function has the same property since it depends only on variables matching this symmetry. Therefore a good fit to a set of experimental cross sections for $\bar{p}$ rapidities above the center of mass rapidity $Y_{c.m.}$ automatically ensures the right behavior of the calculated values for rapidities below $Y_{c.m.}$, i.e., for particle momenta in the laboratory frame, because of the symmetry law.

To conclude this section, the atmospheric $\bar{p}$ fluxes calculated in this work confirm the corrections of the raw flux values measured in the BESS and CAPRICE experiments. This result updates and corrects a previous preliminary conclusion on the issue [53] recently quoted in [64].

The contributions of $A>4$ CR components were not included in the calculations, neither were those from the nonannihilating inelastic contributions in $\bar{p}$ propagation through the atmosphere. These contributions are small, however, and not likely to change the results by more than a few percent [26].

E. AMS altitude

Future satellite experiments in preparation plan to measure the $\bar{p}$ flux. A reliable knowledge of the atmospheric $\bar{p}$ flux at satellite altitudes is therefore highly desirable for these experiments to build on grounds already explored. The $\bar{p}$ fluxes calculated for the altitude of the AMS orbit are presented in this section.

Figure 7 shows the expected downward (secondaries and reentrant albedo, dashed histogram) and upward (splash albedo particles, solid histogram) flux of atmospheric antiprotons at the altitude of AMS for three regions of geomagnetic latitude: equatorial ($0<|\theta_M|<0.2$ rad), intermediate ($0.2<|\theta_M|<0.4$ rad), and subpolar ($0.8<|\theta_M|<0.9$ rad). As expected, the flux is predicted to be larger for the lower latitudes than it is around the poles, because of the existence of quasitrapped $\bar{p}$ components at the low and intermediate latitudes. Note that the simulated flux is surprisingly predicted to be larger downward than upward (bottom left panel). This is in fact an effect of the spectrometer acceptance (taken to be 30° with respect to the zenith), the mean angle for upward particle trajectories being 2 rads. The overall upward flux is larger than the downward by a factor of about 2.5 [43,53]. This shows that future satellite measure-

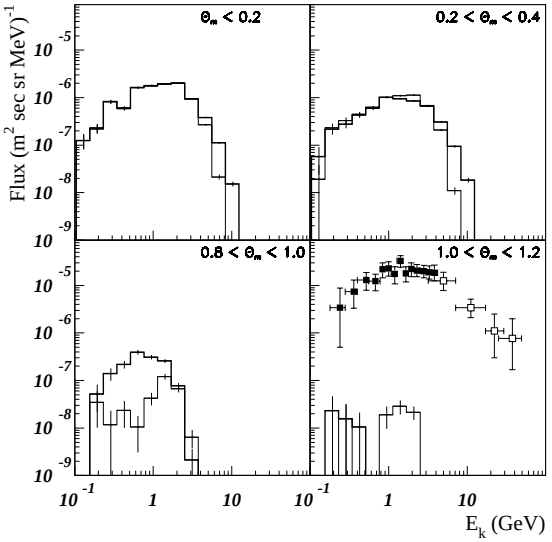

FIG. 7. Atmospheric antiproton spectra expected from the present work for the AMS experiment on the International Space Station at 380 km of altitude for four bins of latitudes, compared with the AMS, BESS, and CAPRICE data [15,16,63] in the polar region (bottom right). Full line: Downward flux. Dashed line: Upward flux. The increasing flux with decreasing latitude is due to the larger (quasi)trapped particle population closer to the equator (see text).

ments of antiproton flux at low latitudes will have to be corrected for the atmospheric contributions and will probably suffer more uncertainties than previously thought.

The lower right panel compares the $\bar{p}$ data at TOA reported by AMS [63], BESS [15], and CAPRICE [13] to the flux calculated in the polar region where the AMS data were measured. The calculated (downward) atmospheric $\bar{p}$ component is at the percent level of the measured flux in the low energy $\bar{p}$ range, and can be considered as negligible at all energies.

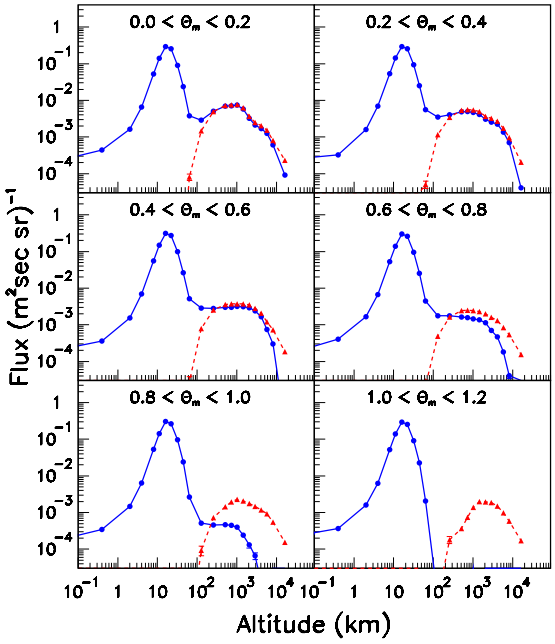

FIG. 9. Integrated antiproton flux versus detection altitude in bins of latitudes between equator and poles, for downward (solid line) and upward (dashed line) $\bar{p}$ flux.

F. $\bar{p}$ and $\bar{n}$ fluxes at terrestrial altitudes

The $\bar{p}$ and $\bar{n}$ fluxes have been calculated at sea level also in order to provide a realistic order of magnitude of these fluxes for general purposes and for ground testing of embarked experiments.

Antiprotons. The flux of atmospheric antiprotons at sea level has been calculated with the same simulation program. Figure 8 shows the distributions obtained at sea level (left) and at 4000 m. The energy integrated flux is of the order of 0.4×10^{-3} $\bar{p}$ s^{-1} m^{-2} sr^{-1} at all latitudes (see Fig. 9 below). At 4000 m (right panel on the figure), the flux increases to

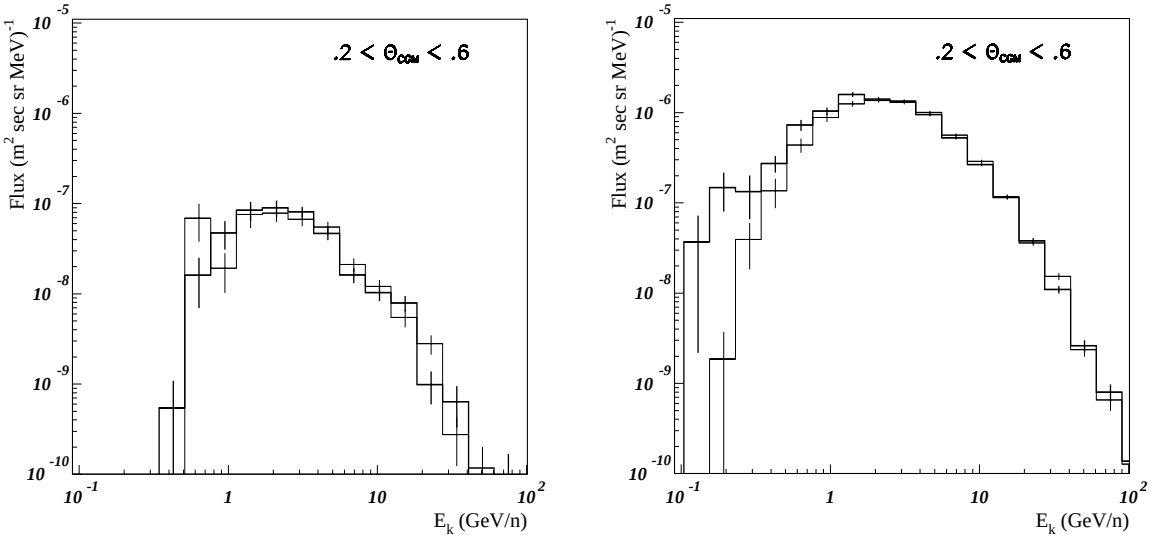

FIG. 8. Simulation results for the antiprotons (thick line) and antineutrons (thin line) flux at sea level (left) and at 4000 m of altitude (right).

about 7×10^{-3} $\bar{p}$ s^{-1} m^{-2} sr^{-1}. These values are small but large enough for this flux to be measured by currently existing large acceptance detectors (BESS, CAPRICE), or in the near future by new detectors under construction (AMS, PAMELA).

Antineutrons. Atmospheric secondary antineutrons may also be of interest in ground or balloon measurements [65]. Figure 8 shows the kinetic energy spectrum of the expected $\bar{n}$ flux at sea level and at 4000 m (this latter altitude being that of the Cerro La Negra Observatory in Mexico, where some experimental measurements of the antineutron flux are being considered [66]).

G. Flux dependence on the altitude

The $\bar{p}$ flux has been calculated up to altitudes of 2×10^4 km with the aim of investigating the general features of the dynamics and kinematics of the particles in more remote earth environments than considered in the previous sections.

Figure 9 shows the altitude dependence of the energy integrated upward and downward $\bar{p}$ flux in bins of latitude, assuming a geometrical acceptance of 30° for the detector. The calculated distributions display two main features.

(1) In the atmospheric range of altitudes, a large peak of incoming flux centered around 20 km and corresponding to atmospheric secondaries dominates the distribution ($\lesssim$50 km, i.e., $\lesssim$ TOA), with basically no associated outgoing flux (inside the quoted acceptance angle).

(2) Above the atmosphere, surprisingly, the calculated upward and downward fluxes are found close to each other up to fairly high altitudes, namely, $\approx10^4$ km, for the low and intermediate latitudes ($|\theta_M|\lesssim0.7$ rad). This shows that a population of quasitrapped particles should be observed in this region of space, i.e., up to around 5000–10000 km. This is confirmed by the lifetime of the particles between their production and their absorption, and by the number of bounces of the particles between the mirror points of their trajectories, which extend up to 100 s and several 10^2 bounces (see Fig. 3), respectively, for the simulation sample produced. At higher latitudes with ($|\theta_M|\gtrsim0.7$ rad), the incoming flux progressively disappears, and the outgoing flux then corresponds to escape particles.

From these calculations it can be concluded that there should exist a significant flux of quasitrapped particles extending approximately over a decade of altitudes, from about 50 km (TOA) up to $\approx10^4$ km, depending on the particle energy and latitude. This flux has been observed already by the AMS experiment in the lower part of the altitude range (380 km) [23]. Note that the issue was discussed long ago in a pioneering paper about the electron flux [57]. See also [22] (companion paper) for a complementary discussion. The energy spectrum of this flux extends up to around 10 GeV, which is about the upper momentum limit (8.5 GeV) for which particles can match the simple geometrical condition that the gyration radius is smaller than the mean trajectory radius to the upper atmosphere (for equatorial latitude trajectories, at the limit of large pitch angles, close to $\pi/2$).

Future experiments should take these features into account, even though, in principle, an accurate knowledge of the kinematical conditions of the particle at the detection point allows one to know whether it is or is not of atmospheric origin.

V. SUMMARY AND CONCLUSION

In summary, the secondary antiproton flux produced by the cosmic ray proton and helium fluxes in the atmosphere has been calculated by Monte Carlo simulation. The flux calculated for the altitude of 2770 m is in fair agreement with the recent BESS measurements. At sea level, it is small but measurable and could provide a natural facility for testing the identification capability of existing experiments or of future devices. For balloon altitudes, the calculated flux has been found to be in agreement with the values calculated in previous work. At satellite altitudes (380 km) it appears to be negligible compared to the CR flux for polar latitudes, and of the same order of magnitude as for the high balloon altitudes for equatorial and intermediate latitudes (below the geomagnetic cutoff), indicating that it will have to be taken into account in future measurements of the galactic antiproton flux at similar altitudes.

ACKNOWLEDGMENTS

The authors are indebted to V. Mikhailov for helpful discussions on the issue and for pointing Ref. [57] to them. They are also grateful to M. Nozaki, M. Fujikawa, and the BESS Collaboration, for providing their measurements of $\bar{p}$ flux at 2770 m prior to publication.

[1] F. Donato *et al.*, Astrophys. J. **563**, 172 (2001).
[2] F.W. Stecker and S. Rudaz, Astrophys. J. **325**, 16 (1988).
[3] A. Bottino *et al.*, Phys. Rev. D **58**, 123503 (1998).
[4] L. Bergström, J. Edsjo, and P. Ullio, in Proceedings of the 26th ICRC, Salt Lake City, Utah, 1999, edited by D. Kieda, M. Salamon, and B. Dingus, High Energy Astrophysics Institute, University of Utah, 1999, astro-ph/9902012.
[5] B. Carr, Astrophys. J. **206**, 8 (1976).
[6] A. Barrau, Astropart. Phys. **12**, 169 (2000), and references therein.
[7] T.K. Gaisser and R.K. Schaefer, Astrophys. J. **394**, 174 (1992).
[8] P. Chardonnet, G. Mignola, P. Salati, and R. Taillet, Phys. Lett. B **384**, 161 (1996).
[9] M. Simon, A. Molnar, and S. Roesler, Astrophys. J. **499**, 250 (1998).
[10] J.W. Bieber *et al.*, Phys. Rev. Lett. **83**, 674 (1999).
[11] P. Ullio, astro-ph/9904086.
[12] I.V. Moskalenko, A.W. Strong, J.F. Ormes, and M.S. Potgieter, Astrophys. J. **565**, 280 (2002).
[13] M. Boezio *et al.*, Astrophys. J. **561**, 787 (2001).

[14] S. Orito *et al.*, Phys. Rev. Lett. **84**, 1078 (2000).
[15] S.T. Maeno *et al.*, Astropart. Phys. **16**, 121 (2001).
[16] M. Boezio *et al.*, Astrophys. J. **487**, 415 (1997).
[17] Ch. Pfeifer, S. Roesler, and M. Simon, Phys. Rev. C **54**, 882 (1996).
[18] T.K. Gaisser *et al.*, in Proceedings of the 26th ICRC, Salt Lake City, Utah, 1999, Vol. 3, p. 69.
[19] D. Maurin, Ph.D. thesis, Université de Savoie, Chambéry, France, 2001.
[20] A.E. Hedin, J. Geophys. Res., [Space Phys.] **96**, 1159 (1991).
[21] J.J. Engelmann *et al.*, Astron. Astrophys. **233**, 96 (1990); W.R. Webber *et al.*, Astrophys. J. **457**, 435 (1996); **508**, 940 (1998).
[22] B. Baret, L. Derome, C.Y. Huang, and M. Buénerd, following paper, Phys. Rev. D **68**, 053009 (2003).
[23] L. Derome *et al.*, Phys. Lett. B **489**, 1 (2000).
[24] L. Derome, Y. Liu, and M. Buénerd, Phys. Lett. B **515**, 1 (2001).
[25] L. Derome and M. Buénerd, Phys. Lett. B **521**, 139 (2001).
[26] Yong Liu, L. Derome, and M. Buénerd, Phys. Rev. D **67**, 073022 (2003).
[27] AMS Collaboration, J. Alcaraz *et al.*, Phys. Lett. B **472**, 215 (2000); **490**, 27 (2000).
[28] AMS Collaboration, J. Alcaraz *et al.*, Phys. Lett. B **494**, 19 (2000).
[29] M. Boezio *et al.*, Astrophys. J. **518**, 457 (1999).
[30] W. Menn *et al.*, Astrophys. J. **533**, 281 (2000).
[31] T. Sanuki *et al.*, Astrophys. J. **545**, 1135 (2000).
[32] J.S. Perko, Astron. Astrophys. **184**, 119 (1984); see M.S. Potgieter, in Proceedings of the ICRC, Calgary, 1993, p. 213, for a recent review of the subject.
[33] K. Goulianos, Phys. Rep. **101**, 169 (1983).
[34] Y.D. Bayukov *et al.*, Sov. J. Nucl. Phys. **42**, 116 (1985).
[35] T. Abbott *et al.*, Phys. Rev. D **45**, 3906 (1992).
[36] A. Boudard, J. Cugnon, S. Leray, and C. Volant (unpublished).
[37] Y. Sugaya *et al.*, Nucl. Phys. **A634**, 115 (1998).
[38] T. Abbott *et al.*, Phys. Rev. C **47**, 1351 (1993).
[39] J. V. Allaby *et al.*, Report No. CERN/70-12, 1970.
[40] T. Eichten *et al.*, Nucl. Phys. **B44**, 333 (1972).
[41] A.N. Kalinovski, M.V. Mokhov, and Yu.P. Nikitin, *Passage of High Energy Particles Through Matter* (AIP, New York, 1989), Chap. 3.
[42] C.Y. Huang and M. Buénerd, Report No. ISN 01-018, 2001.
[43] C.Y. Huang, Ph.D. thesis, Université J. Fourier, Grenoble, France, 2002.
[44] R. Duperray, C.Y. Huang, K. Protasov, and M. Buénerd, astro-ph/0305274.
[45] J. Jaros *et al.*, Phys. Rev. C **18**, 2273 (1978).
[46] D. Armutliiski *et al.*, Sov. J. Nucl. Phys. **45**, 649 (1987).
[47] S. Baskovic *et al.*, Phys. At. Nucl. **56**, 540 (1993).
[48] A. Bialas, M. Bleszynski, and C.W. Czyz, Nucl. Phys. **B111**, 461 (1976).
[49] M.A. Faessler, Phys. Rep. **115**, 1 (1984).
[50] J.R. Letaw, R. Silberberg, and C.H. Tsao, Astrophys. J., Suppl. Ser. **51**, 271 (1983).
[51] A.S. Carroll *et al.*, Phys. Lett. **80B**, 319 (1979); C. Denisov *et al.*, Nucl. Phys. **B61**, 62 (1973); K. Nakamura *et al.*, Phys. Rev. Lett. **52**, 731 (1984); C. Barbina *et al.*, Nucl. Phys. **A612**, 346 (1997).
[52] A. Baldini *et al.*, in *Numerical Data and Functional Relationships in Science and Technology*, edited by K.-H. Hellwege and A.M. Hellwege, Landolt-Börnstein, New Series, Vol. I/12b (Springer-Verlag, Berlin, 1988).
[53] C.Y. Huang *et al.*, in Proceedings of the 27th ICRC, Hamburg, 2001.
[54] S.F. Singer and A.M. Lenchek, Prog. Elem. Part. Cosmic Ray Phys. **6**, 245 (1962).
[55] C. Störmer, *The Polar Aurora* (Clarendon Press, Oxford, 1955).
[56] R. Gall and J. Lifschitz, in Proceedings of the IUPAP Cosmic Ray Conference, Moscow, 1960, edited by S.I. Syrovatsky, University of Moscow, Vol. 3, p. 64.
[57] N.L. Grigorov, Sov. Phys. Dokl. **22**, 305 (1977).
[58] M. Buénerd, Int. J. Mod. Phys. A **17**, 1665 (2002).
[59] T. Sanuki *et al.*, in Proceedings of the 28th ICRC, Tsukuba, Japan, 2003, astro-ph/0305529; astro-ph/0306582.
[60] M. Fujikawa, Ph.D. thesis, University of Tokyo, 2001.
[61] S.A. Stephens, Astropart. Phys. **6**, 229 (1997).
[62] Y. Ajima *et al.*, Nucl. Instrum. Methods Phys. Res. A **443**, 71 (2000); Y. Asao *et al.*, *ibid.* **416**, 236 (1998).
[63] AMS Collaboration, J. Alcaraz *et al.*, Phys. Rep. **336**, 331 (2002).
[64] I.V. Moskalenko, A.W. Strong, S.G. Mashnik, and J.F. Ormes, Astrophys. J. **586**, 1050 (2003); LANL-REPORT-LA-UR-02-7813, 2003, astro-ph/0301450.
[65] A. Menchaca-Rocha (private communication).
[66] See http://www.auger.unam.mx/cln/